

Formulae and Software for Particular Solutions to the Elastic Wave Equation in Curved Geometries

Kristoffer Virta^{a,*}, Daniel Appelö^{b,1}

^a*Division of Scientific Computing, Department of Information Technology,
Uppsala University, Box 337, 75105 Uppsala, Sweden.*

^b*Department of Mathematics and Statistics, University of New Mexico,
1 University of New Mexico, Albuquerque, NM 87131.*

Abstract

We present formulae for particular solutions to the elastic wave equation in cylindrical geometries. We consider scattering and diffraction from a cylinder and inclusion and surface waves exterior and interior to a cylindrical boundary. The solutions are used to compare two modern numerical methods for the elastic wave equation. Associated to this paper is the free software **PeWe** that implements the exact solutions.

Keywords: elastic wave equation, exact solutions, curved geometries, scattering and diffraction, surface waves, SBP-SAT, discontinuous Galerkin method

1. Introduction

Pressure and shear waves associated with seismic events in the Earth as well as waves in plates, beams and solid structures are governed by the elastic wave equation. The domain in which the waves are traveling is in general of finite extension in at least one spatial direction and may contain material heterogeneities. This introduces conditions at the boundaries of the domain and at interfaces between differing materials that a solution must satisfy. Two frequently occurring conditions are the vanishing of stress at a boundary and the continuity of displacement and stress at a material interface. The former appears for example at the surface of the Earth and the later at internal interfaces due to its layered structure. A distinguishing characteristic of the interaction between elastic waves and boundaries or interfaces is that mode conversion occurs. That is, when a wave, either pressure or shear, impinges on a boundary or interface it is converted into both shear and pressure waves upon reflection. Disturbances at boundaries or interfaces may generate a wave that clings to the boundary or interface and travels independent of the pressure and shear waves. In general domains boundaries and interfaces are non-planar. A curved geometry has a radius of curvature which introduces a length scale that

*Corresponding author

Email addresses: `kristoffer.virta@it.uu.se` (Kristoffer Virta), `appel@math.unm.edu` (Daniel Appelö)

¹Supported in part by NSF Grant DMS-1319054. Any conclusions or recommendations expressed in this paper are those of the author and do not necessarily reflect the views NSF.

Preprint submitted to Journal of Computational Physics

August 28, 2015

may differ from that of the scales represented by the present wavelengths, this gives rise to dispersion and possibly attenuation in solutions. A planar boundary or interface does not have this feature. The effect of curvature, existence of boundary and interface waves and mode conversion at boundaries and interfaces account for the relative complexity of wave motion in elastic solids compared to similar problems in acoustics.

The complexity of elastic wave propagation makes a numerical solution of the elastic wave equation appealing and a lot of research is devoted to the design of stable, accurate and efficient methods. Preferably a numerical method should be able to handle complex geometries as well as boundary and interface conditions. To ascertain the quality and correctness of a numerical solution a comparison with a known solution should be performed. The known solution can be found in some different ways. For example, the known solution can be constructed by the manufactured solution technique where a function, e.g. a trigonometric polynomial, is chosen and inserted into the equation. As the function does not satisfy the equation, boundary and interior forcing are added so that the function is instead a solution to a modified, forced problem. This method verifies that the numerical scheme is stable and accurate. A manufactured solution is however unphysical and does not test the capability of the numerical method to handle the various physical phenomena that arise at boundaries and interfaces.

Another approach is to use a reference solution as the known solution. Now, a numerical solution with given data is computed using a computational grid with a small discretization length. This solution is considered exact and comparisons are made with numerical solutions computed on coarser grids. This method is unappealing, for every set of data a solution that requires substantial computational power and time is needed and, regardless of the resolution of the reference solution, it is still only an approximate solution. In addition the use of a reference solution does not eliminate the possibility that the discretized equations may not be the same as the equations one set out to solve in the first place.

A third approach to constructing known solutions is to solve the equations exactly by separation of variables techniques. When the domain of interest contains planar boundaries or interfaces, time-harmonic exact solutions to the elastic wave equation that exhibits typical boundary or interface behavior are easily obtained using plane wave analysis [2]. Also, boundary value problems involving transient time behavior have been studied. The archetype being Lamb's problem first introduced by Lamb, [3], in which the boundary of an elastic half-plane is being subjected to a transient load in the direction normal to the surface. Exact solutions to variations of Lamb's problem have been presented by Mooney [4] and latter used to evaluate the performance of a numerical methods in [5]. Exact solutions to problems involving internal sources in three dimensional, layered media was used by Day et.al., [6] to give a systematic comparison of the performance of different numerical codes that solve the elastic wave equation.

In recent years a number of new methods for the elastic wave equation has been presented [7–15] however there has been a dearth in open source software providing exact solutions that can be used for validating the correctness and benchmarking the performance of old and new methods. In the context of seismology the notable exceptions is the monograph by Kausel [16], the suite EX2DDIR/EX2DELEL/EX2DVAEL by Berg et al. [17] and the program Gar6more 2D/3D by Diaz and Ezziani, [18]. The latter two methods rely on the Cagniard-de-Hoop technique and are restricted to planar / layered geometries including point sources. Nowadays most of the numerical methods are capable

to handle curved geometries and we therefore focus here on developing exact solutions and software for the homogenous (un-forced) equations in cylindrical geometries with free boundaries and internal interfaces. Our hope is that these solutions and associated software, freely available from [1], will augment existing open source software.

Solutions representing surface waves at the convex boundary of a circular cylinder was first investigated by Sezawa [19]. Sezawa showed how the effect of curvature enter into the dispersion relations. The solutions were described in terms of Bessel functions of the first kind, for this reason a numerical solution in the general case requires availability of numerical values of Bessel functions of the first kind with sufficient accuracy for an arbitrary argument. A qualitative diagram that illustrates the dispersive nature of the surface wave was given by Sezawa for the case $\lambda = \mu$, where λ is Lamé's first parameter and μ is the shear modulus, but no numerical values were presented.

The change in nature of surface waves on the concave boundary of a circular cylinder in that the wave is now attenuated was discussed by Epstein [20]. The dispersion relation governing the phase velocity now involves Hankel functions of complex order, which was remarked by Epstein to make computations more involved. In this paper we circumvent this difficulty by instead expressing the solutions in terms of Hankel functions of integer order but with a complex argument which makes it easier to find roots of the corresponding dispersion relation using numerical methods.

Exact solutions that represent scattering by a spherical cavity or inclusion resulting from an incident plane pressure wave have been constructed by Pao and Mow [21]. The incoming, scattered and diffracted waves were represented by Fourier series expansions, with coefficients determined to fulfill the boundary or interface conditions at the surface of the sphere. This approach was also used by Miles [22] to study a plane pressure or shear wave impinging on a rigid circular cylindrical body, here the boundary conditions at the cylinder differ from the ones mentioned above.

The goal of this paper is to make available to computational scientists exact solutions to the elastic wave equation that represent physical phenomena occurring at boundaries and interfaces in curved geometries. These exact solutions are presented in terms of formulas that can be evaluated, using supplied software (freely available), to generate initial and boundary data. The supplied routines can also be used to compute errors in the numerical solution at any given time and point in space.

In this paper we present the solutions to four different problems:

- Scattering by a circular cylindrical cavity in an elastic medium,
- Scattering and diffraction by a circular cylindrical inclusion in an elastic medium,
- Surface waves on the convex boundary of an elastic circular cylinder,
- Surface waves on the concave boundary of a circular cylindrical cavity in an elastic medium.

The derivation of solutions representing the first two cases is inspired by [21] in that the same technique is used but here the scatterer is an infinite circular cylinder, thus reducing the number of relevant spatial dimensions to two. The derivation of solutions representing the last two cases follows the work of Sezawa [19] and Epstein [20] but complementing these works with numerical parameters necessary to use these particular solutions in actual numerical computations. Numerical values of the present parameters

are presented in Appendix B. As an illustration of the usage of the particular solutions, we present numerical results using two methods. The first method is based on finite differences, the second method is based on the discontinuous Galerkin method. The finite difference method requires a structured grid while the discontinuous Galerkin method handles unstructured grids. For ease of comparison we use the same grids for both methods in our computations, the construction of the grids are described in detail to facilitate future computations with other methods.

2. The Elastic Wave Equation in Cylindrical Geometries

Consider a circular cylinder enclosed in an infinite surrounding medium. The radius of the cylinder is $a > 0$ and its axis is parallel to one of the coordinate axes, say z . We consider the case when the material properties of the cylinder and the surrounding medium are different and we allow for either to be a vacuum. The displacement in the direction of the cylindrical axis is omitted, the remaining radial and azimuthal components of the displacement, $p(r, \theta, t)$ and $q(r, \theta, t)$, are functions of the cylindrical coordinates, r and θ and can be expressed as

$$\begin{aligned} p &= \phi_r + \frac{1}{r}\psi_\theta, \\ q &= \frac{1}{r}\phi_\theta - \psi_r, \end{aligned} \tag{1}$$

where ϕ and ψ solve the wave equations

$$\rho\phi_{tt} = c_p^2 \left(\frac{1}{r}\phi_r + \phi_{rr} + \frac{1}{r^2}\phi_{\theta\theta} \right), \tag{2}$$

$$\rho\psi_{tt} = c_s^2 \left(\frac{1}{r}\psi_r + \psi_{rr} + \frac{1}{r^2}\psi_{\theta\theta} \right). \tag{3}$$

Here

$$c_p = \sqrt{\frac{\lambda + 2\mu}{\rho}}, c_s = \sqrt{\frac{\mu}{\rho}}, \tag{4}$$

ρ is the density of the elastic medium, λ is Lamé's first parameter and μ is the shear modulus. The functions ϕ and ψ represent pressure and shear waves propagating with phase velocities c_p and c_s , respectively. In Cartesian coordinates $x = r \cos(\theta)$ and $y = r \sin(\theta)$ and the horizontal and vertical displacement components $u(x, y, t)$ and $v(x, y, t)$ are given by

$$\begin{aligned} u(x, y, t) &= \cos(\theta)p(r, \theta, t) - \sin(\theta)q(r, \theta, t), \\ v(x, y, t) &= \sin(\theta)p(r, \theta, t) + \cos(\theta)q(r, \theta, t). \end{aligned} \tag{5}$$

If the surrounding media or the cylinder is a vacuum no wave motion occurs in the vacuum and the surface of the cylinder is free of traction. This is described by the boundary conditions

$$\begin{aligned} \lambda \left(p_r(a, \theta, t) + \frac{1}{r}q_\theta(a, \theta, t) + \frac{1}{r}p(a, \theta, t) \right) + 2\mu p_r(a, \theta, t) &= 0, \\ \mu \left(\frac{1}{r}p_\theta(a, \theta, t) + q_r(a, \theta, t) - \frac{1}{r}q(a, \theta, t) \right) &= 0. \end{aligned} \tag{6}$$

When there is no vacuum the normal and tangential components of the displacement and stress tensor are required to be continuous across the interface, $r = a$, between the two materials. Let the quantities inside the cylinder be denoted with a prime, then the interface conditions take the form

$$\begin{aligned}
p(a, \theta, t) &= p'(a, \theta, t), \\
q(a, \theta, t) &= q'(a, \theta, t), \\
(\lambda + 2\mu)p_r(a, \theta, t) + \frac{\lambda}{a}(q_\theta(a, \theta, t) + p(a, \theta, t)) &= \\
(\lambda' + 2\mu')p'_r(a, \theta, t) + \frac{\lambda'}{a}(q'_\theta(a, \theta, t) + p'(a, \theta, t)), \\
\mu(p_\theta(a, \theta, t) + aq_r(a, \theta, t) - q(a, \theta, t)) &= \\
\mu'(p'_\theta(a, \theta, t) + aq'_r(a, \theta, t) - q'(a, \theta, t)).
\end{aligned} \tag{7}$$

3. Particular Solutions to the Elastic Wave Equation

In this section two types of particular solutions to the elastic wave equation are derived. The first type describes the scattering of an incident pressure wave striking a cylindrical cavity or inclusion. In the first case the interior of the cylinder is a vacuum and its boundary is free of traction. In the second case the interior of the cylinder is of a material differing from the surrounding medium and continuity of displacements as well as tractions are required at the boundary of the cylinder. The second type of solutions relates to waves propagated on the surface of the cylinder. In this case a distinction is made between waves traveling on the convex boundary of the interior of the cylinder, the surrounding media being a vacuum, or the concave exterior of the cylinder, its interior being a vacuum.

3.1. Scattering and Diffraction of Pressure Waves by a Cylindrical Cavity or Inclusion

Consider an incident time-harmonic plane compressional wave

$$\phi^{(i)}(r, \theta, t) = \phi_0 e^{i(\omega t - \gamma_p r \cos(\theta))}, \quad \phi_0 = \text{constant}, \tag{8}$$

traveling in the direction $\theta = 0$. When the wave strikes the cylindrical cavity or inclusion mode conversion occurs, i.e., the reflections will consist of both pressure waves $\phi^{(s)}$ and shear waves $\psi^{(s)}$. In the case of an inclusion the diffracted waves will also consist of pressure and shear waves, $\phi^{(d)}$ and $\psi^{(d)}$ respectively. The total incident and reflected displacement fields in $r > a$ are given by (1) as

$$\begin{aligned}
p &= \phi_r^{(i)} + \phi_r^{(s)} + \frac{1}{r}\psi_\theta^{(s)}, \\
q &= \frac{1}{r} \left(\phi_\theta^{(i)} + \phi_\theta^{(s)} \right) - \psi_r^{(s)}.
\end{aligned} \tag{9}$$

The total diffracted displacement fields inside the inclusion, $r < a$, are given by

$$\begin{aligned}
p' &= \phi_r'^{(d)} + \frac{1}{r}\psi_\theta'^{(d)}, \\
q' &= \frac{1}{r}\phi_\theta'^{(d)} - \psi_r'^{(d)}.
\end{aligned} \tag{10}$$

The incident wave automatically solves equation (2) when $\gamma_p = \omega/c_p$.

Since the wave equation is separable in cylindrical coordinates the ansatz

$$\phi^{(s)} = R\Theta e^{i\omega t}, \quad (11)$$

separates equation (2) into

$$\begin{aligned} \frac{d^2}{d\theta^2}\Theta + k^2\Theta &= 0, \\ \frac{d^2}{dr^2}R + \frac{1}{r} + \left(\gamma_p^2 - \frac{k^2}{r^2}\right)R &= 0. \end{aligned} \quad (12)$$

The solutions to (12) are

$$\Theta = A \cos(k\theta) + B \sin(k\theta), \quad (13)$$

$$R = CH_k^{(1)}(\gamma_p r) + DH_k^{(2)}(\gamma_p r), \quad (14)$$

where $H_k^{(1)}$ and $H_k^{(2)}$ are Hankel functions of the first and second kind, respectively. Symmetry with respect to the x -axis requires $B = 0$ in (13) and requiring that Θ be single-valued ($\Theta(\theta) = \Theta(\theta + 2\pi)$) indicates that k is an integer say $k = n$.

For large values of the argument the Hankel functions have the asymptotic expansions

$$H_n^{(1)}(z) \approx \left(\frac{2}{\pi z}\right)^{1/2} e^{i(z - \frac{\pi}{4} - \frac{ka\pi}{2})} (1 - \dots), \quad (15)$$

$$H_n^{(2)}(z) \approx \left(\frac{2}{\pi z}\right)^{1/2} e^{-i(z - \frac{\pi}{4} - \frac{ka\pi}{2})} (1 + \dots). \quad (16)$$

Since the time dependence is $e^{i\omega t}$ an outward propagating wave must have the form $e^{i(\omega t - \gamma_p r)}$ so taking $C = 0$ in (14) is appropriate for the present case. The scattered pressure wave field is thus given by a superposition of solutions of the form (11)

$$\phi^{(s)}(r, \theta, t) = e^{i\omega t} \sum_{n=0}^{\infty} A_n H_n^{(2)}(\gamma_p r) \cos(n\theta), \quad r > a. \quad (17)$$

By the same reasoning the scattered shear wave field may be written

$$\psi^{(s)}(r, \theta, t) = e^{i\omega t} \sum_{n=0}^{\infty} B_n H_n^{(2)}(\gamma_s r) \sin(n\theta), \quad r > a, \quad (18)$$

where $\gamma_s = \omega/c_s$.

The diffracted wave fields are defined inside the cylindrical inclusion and are required to be bounded at the origin. For this reason the Hankel function in the expression (14) for the corresponding R is replaced by the Bessel function of the first kind. The resulting solutions inside $r < a$ are written as

$$\begin{aligned} \phi'^{(d)}(r, \theta, t) &= e^{i\omega t} \sum_{n=0}^{\infty} C_n J_n(\gamma'_p r) \cos(n\theta), \\ \psi'^{(d)}(r, \theta, t) &= e^{i\omega t} \sum_{n=0}^{\infty} D_n J_n(\gamma'_s r) \sin(n\theta), \end{aligned} \quad (19)$$

where quantities with primes relate to those defined inside the cylindrical inclusion. To match expressions term by term we write the incident wave $\phi^{(i)}$ in Bessel functions of the first kind using the identity

$$e^{-i\gamma_p r \cos(\theta)} = \sum_{n=0}^{\infty} (\epsilon_n (-i)^n J_n(\gamma_p r) \cos(n\theta)), \quad (20)$$

where

$$\begin{cases} \epsilon_0 = 1, \\ \epsilon_n = 2, n \geq 1. \end{cases}$$

By (9) the radial and azimuthal components, representing the incident and scattered fields in $r > a$, are given by

$$\begin{aligned} p(r, \theta, t) &= e^{i\omega t} \sum_{n=0}^{\infty} \left(\phi_0 \epsilon_n (-i)^n \frac{d}{dr} J_n(\gamma_p r) \right. \\ &\quad \left. + A_n \frac{d}{dr} H_n^{(2)}(\gamma_p r) + B_n \frac{n}{r} H_n^{(2)}(\gamma_s r) \right) \cos(n\theta), \\ q(r, \theta, t) &= e^{i\omega t} \sum_{n=0}^{\infty} \left(\frac{-n}{r} \phi_0 \epsilon_n (-i)^n J_n(\gamma_p r) \right. \\ &\quad \left. + A_n \frac{-n}{r} H_n^{(2)}(\gamma_p r) - B_n \frac{d}{dr} H_n^{(2)}(\gamma_s r) \right) \sin(n\theta). \end{aligned} \quad (21)$$

Solutions that represent the diffracted fields in $r < a$ are given via (10) by

$$\begin{aligned} p'(r, \theta, t) &= e^{i\omega t} \sum_{n=0}^{\infty} \left(C_n \frac{d}{dr} J_n(\gamma_p' r) + D_n \frac{n}{r} J_n(\gamma_s' r) \right) \cos(n\theta), \\ q'(r, \theta, t) &= e^{i\omega t} \sum_{n=0}^{\infty} \left(C_n \frac{-n}{r} H_n^{(2)}(\gamma_p' r) - D_n \frac{d}{dr} J_n(\gamma_s' r) \right) \sin(n\theta). \end{aligned} \quad (22)$$

In the case of a cylindrical cavity no wave motion occurs inside the cylinder and $C_n = D_n = 0$ in (22). The coefficients A_n and B_n of (21) are determined by substituting the solutions (21) into the boundary conditions (6) and equating coefficients of $\cos n\theta$ and $\sin n\theta$ in virtue of Fourier's method. This results in the linear systems

$$\begin{bmatrix} m_n^{(11)} & m_n^{(12)} \\ m_n^{(21)} & m_n^{(22)} \end{bmatrix} \begin{bmatrix} A_n \\ B_n \end{bmatrix} = \phi_0 \epsilon_n (-i)^{n+1} \begin{bmatrix} f_n^{(1)} \\ f_n^{(2)} \end{bmatrix}, \quad n = 1, 2, \dots, \quad (23)$$

for the coefficients A_n and B_n . Exact expressions for arbitrary values of ρ , λ and μ of the coefficients $m_n^{(ij)}$ and $f_n^{(i)}$, $i = 1, 2$, $j = 1, 2$, $n = 1, 2, \dots$, are presented in Appendix A.

Similarly, inserting the solutions (21)-(22) into the interface conditions (7) and equating coefficients of $\cos n\theta$ and $\sin n\theta$ results in the linear systems

$$\begin{bmatrix} m_n^{(11)} & m_n^{(12)} & m_n^{(13)} & m_n^{(14)} \\ m_n^{(21)} & m_n^{(22)} & m_n^{(23)} & m_n^{(24)} \\ m_n^{(31)} & m_n^{(32)} & m_n^{(33)} & m_n^{(34)} \\ m_n^{(41)} & m_n^{(42)} & m_n^{(43)} & m_n^{(44)} \end{bmatrix} \begin{bmatrix} A_n \\ B_n \\ C_n \\ D_n \end{bmatrix} = \phi_0 \epsilon_n (-i)^{n+1} \begin{bmatrix} f_n^{(1)} \\ f_n^{(2)} \\ f_n^{(3)} \\ f_n^{(4)} \end{bmatrix}, \quad n = 1, 2, \dots, \quad (24)$$

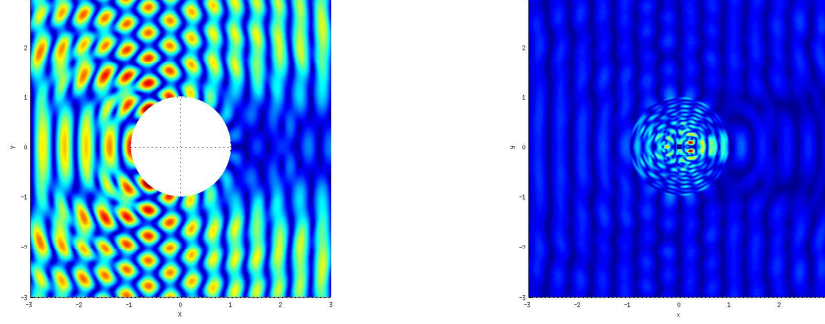


Figure 1: Particular solutions that represent scattering by a cylindrical cavity with material parameters $\lambda = \mu = \rho = 1$, (left) and diffraction by a cylindrical inclusion with material parameters $\lambda = \mu = \rho = 1$, $\lambda' = 1/2$, $\mu' = 1/10$, $\rho' = 1$ (right).

for the coefficients A_n, B_n, C_n, D_n . Exact expressions for arbitrary values of ρ , λ and μ of the coefficients $m_n^{(ij)}$ and $f_n^{(i)}$, $i = 1, 4, j = 1, 4, n = 1, 2, \dots$, are presented in Appendix A.

Figure 1 displays the magnitude of the displacement field given by the solutions (21)-(22). Here the series have been truncated when the coefficients A_n, B_n, C_n, D_n are smaller than roundoff.

3.2. Surface Waves on the Convex or Concave Boundary of a Cylinder

Particular solutions of equations (2)-(3) that represent time - harmonic circumferential waves that travel in the tangential direction along boundary of the cylinder with phase velocity c are

$$\begin{aligned}\phi(r, \theta) &= AF_{ka}(c\eta_p r)e^{ika(ct+\theta)} \\ \psi(r, \theta) &= BF_{ka}(c\eta_s r)e^{ika(ct+\theta)}.\end{aligned}\tag{25}$$

Here

$$\eta_p = \frac{ka}{\sqrt{\lambda + 2\mu}}, \quad \eta_s = \frac{ka}{\sqrt{\mu}},\tag{26}$$

and $F_n(z)$ denotes either a Bessel function or a Hankel function. The radial and azimuthal displacements becomes

$$\begin{aligned}p(r, \theta, t) &= \left(A \frac{dF_{ka}(c\eta_p r)}{dr} + B \frac{ika}{r} F_{ka}(c\eta_s r) \right) e^{ika(ct+\theta)}, \\ q(r, \theta, t) &= \left(A \frac{ika}{r} F_{ka}(c\eta_p r) - B \frac{dF_{ka}(c\eta_s r)}{dr} \right) e^{ika(ct+\theta)}.\end{aligned}\tag{27}$$

Continuity requires that $ka = n$, with n being an integer, and boundedness in time requires that $\Im c \geq 0$.

In the case of a surface wave at the convex boundary of a circular cylinder (inside the cylinder) a solution that is bounded at the origin is required, thus $F_{ka} = J_{ka}$ is appropriate in this case.

To describe a surface wave traveling along the concave boundary of a cylindrical cavity we set $F_{ka} = H_{ka}^{(2)}$, the Hankel function of the second kind. Far away from the cylinder the asymptotic expansion (16) hold and $\phi \sim e^{ic(kat - \eta_p r)}$, $\psi \sim e^{ic(kat - \eta_s r)}$. Hence, if $\Im c > 0$, surface waves on the concave boundary of the cylinder are being attenuated, the attenuation is due to energy being propagating outward from the boundary of the cylinder.

Inserting the solutions (27) into the boundary conditions (6) at $r = a$ results in the following homogeneous system of equations with unknowns A and B ,

$$\begin{aligned} -\mu \left(c^2 (\eta_s^2 - 2\eta_p^2) F_{ka}(c\eta_p a) - 2 \frac{d^2 F_{ka}(c\eta_p a)}{dr^2} \right) A \\ + 2\mu i k \left(\frac{dF_{ka}(c\eta_s a)}{dr} - \frac{F_{ka}(c\eta_s a)}{a} \right) B = 0, \end{aligned} \quad (28)$$

$$\begin{aligned} 2\mu i k \left(\frac{dF_{ka}(c\eta_p a)}{dr} - \frac{F_{ka}(c\eta_p a)}{a} \right) A \\ + \mu \left((c^2 \eta_s^2 - 2k^2) F_{ka}(c\eta_s a) + \frac{2}{a} \frac{dF_{ka}(c\eta_s a)}{dr} \right) B = 0. \end{aligned} \quad (29)$$

A solution exists if and only if there is a phase velocity c such that the determinant of the system (28)-(29)

$$\begin{aligned} D(c) = \frac{-1}{\mu^2} \left(c^2 (\eta_s^2 - 2\eta_p^2) F_{ka}(c\eta_p a) - 2 \frac{d^2 F_{ka}(c\eta_p a)}{dr^2} \right) \\ \times \left((c^2 \eta_s^2 - 2k^2) F_{ka}(c\eta_s a) + \frac{2}{a} \frac{dF_{ka}(c\eta_s a)}{dr} \right) \\ - 4k^2 \left(\frac{dF_{ka}(c\eta_p a)}{dr} - \frac{F_{ka}(c\eta_p a)}{a} \right) \left(\frac{dF_{ka}(c\eta_s a)}{dr} - \frac{F_{ka}(c\eta_s a)}{a} \right), \end{aligned} \quad (30)$$

vanishes. Note that unlike the Rayleigh wave at a planar boundary, the surface wave on a curved boundary is dispersive, i.e. the phase velocity $c = c(k)$ depends on the wave number k .

3.3. Computing Phase Velocities

Explicit usage of the expressions (27) requires knowledge of the location of a zero c of the determinant (30). Surface waves on the convex or concave boundary of the cylinder are represented by taking $F_{ka} = J_{ka}$ or $F_{ka} = H_{ka}^{(2)}$ in (30), respectively. In both cases it is required that ka is an integer in order for the solution to be single-valued. The Bessel function of the first kind J_{ka} is real valued for real arguments when the order is an integer but the Hankel function of the second kind $H_{ka}^{(2)}$ may have a non-negative imaginary part for any argument. For this reason real zeros of the determinant (30) are sought when considering surface waves on a convex boundary and complex-valued zeros with $\Im c > 0$ are sought when considering surface waves on a concave boundary. Numerical methods was used to find zeros with 16 digits accuracy. In both cases the zeros are seen to be non-unique. That is, for each wave number a multitude of phase velocities exists. Tables B.2 and B.3 displays some computed values of c for both cases.

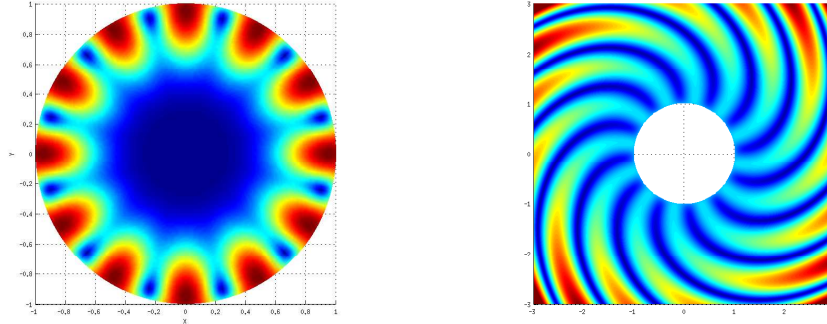


Figure 2: Particular solutions that represent surface waves at the convex (left) or concave boundary of a cylinder (right). In both figures the material parameters are $\lambda = \mu = \rho = 1$.

4. Numerical Methods and Grid Generation

This section briefly presents the numerical methods used and gives a detailed description of the grids used in the computations. The detailed description of the grids used should facilitate future comparison with other numerical methods.

As mentioned in the introduction the solutions we use here are freely available in the open source software **PeWe** which can be obtained at [1]. Examples of how **PeWe** can be used in Matlab and Fortran programs are also given at [1].

4.1. The Finite-Difference Method

The finite-difference method used in the following experiments was developed by Duru et.al., [12, 13]. It is based on discretizing the elastic wave equation in two spatial dimensions written as the second order system

$$\begin{aligned} u_{tt} &= \mu \Delta u + (\lambda + \mu)(u_x + v_y)_x, \\ v_{tt} &= \mu \Delta v + (\lambda + \mu)(u_x + v_y)_y, \end{aligned} \quad (31)$$

where u and v are the vertical and horizontal displacement components, respectively. The spatial discretization uses high order finite difference operators that satisfies a summation-by-parts (SBP) rule [23, 24]. Boundary and interface conditions are imposed weakly via the simultaneous-approximation-term (SAT) method [25]. With the SBP-SAT methodology the local order of accuracy at a grid point in the interior of the computational domain is in general $2p$, where p is an integer. In the vicinity of a boundary or interface the order of accuracy decreases to p . When discretizing a second-order hyperbolic system with the SBP-SAT methodology it can be shown, [26], that the global order of accuracy is $p + 2$. The finite difference method used in this paper has $p = 3$, resulting in a fifth order accurate method.

4.2. The Discontinuous Galerkin Method

The discontinuous Galerkin method, described in detail in [27], is designed to mimic the dynamics of the elastic energy of the system. The method discretizes the the first

order system (in time)

$$\begin{aligned} u_t &= \dot{u}, \\ v_t &= \dot{v}, \\ \dot{u}_t &= \mu \Delta u + (\lambda + \mu)(u_x + v_y)_x, \\ \dot{v}_t &= \mu \Delta v + (\lambda + \mu)(u_x + v_y)_y, \end{aligned} \tag{32}$$

by a variational formulation where the first two equations are tested against the variational derivative of the potential energy density

$$G = \frac{\lambda}{2} \left(\frac{\partial u}{\partial x} + \frac{\partial v}{\partial y} \right)^2 + \frac{2\mu}{2} \left(\left(\frac{\partial u}{\partial x} \right)^2 + \left(\frac{\partial v}{\partial y} \right)^2 + \frac{1}{2} \left(\frac{\partial u}{\partial y} + \frac{\partial v}{\partial x} \right)^2 \right). \tag{33}$$

The formulation in [27] allows for both energy conserving fluxes and fluxes of upwind type, here we exclusively use the upwind-type. Further the formulation in [27] allows for different approximation spaces for the displacement and velocity. Here we choose both the approximation spaces to be tensor product polynomials of degree q which, when used together with the upwind flux, results in a method that is of order $q + 1$ in space. For the evolution in time we use the classic fourth order accurate Runge-Kutta method. An open source implementation of the discontinuous Galerkin solver can be obtained from [28].

4.3. Grid Generation

The particular solutions presented in this paper are defined on three different two-dimensional domains,

- \mathcal{D}_1 : the interior of a cylinder of radius a ,
- \mathcal{D}_2 : the exterior of a cylinder of radius a ,
- \mathcal{D}_3 : a whole elastic plane with a cylindrical inclusion of a differing material and radius a .

Here we present a description of how the grids used in the following experiments are constructed. Examples of the grids can be found in Figure 3.

The domains are handled by decomposing each domain in a multi-block fashion. The domain \mathcal{D}_1 is split into five blocks and the domain \mathcal{D}_2 is split into four. The domain \mathcal{D}_3 is discretized by a grid consisting of the union of the grids discretizing \mathcal{D}_1 and \mathcal{D}_2 .

To this end, let $(\xi, \eta) \in [0, 1]^2 = \mathcal{S}$ be the coordinates of the unit square. All blocks \mathcal{B}_i have four boundaries defined by parametrized curves

$$\begin{aligned} \mathcal{C}_{iS} &= (x_{iS}(\xi), y_{iS}(\xi)), & \mathcal{C}_{iN} &= (x_{iN}(\xi), y_{iN}(\xi)), \\ \mathcal{C}_{iW} &= (x_{iW}(\eta), y_{iW}(\eta)), & \mathcal{C}_{iE} &= (x_{iE}(\eta), y_{iE}(\eta)), \end{aligned}$$

where \mathcal{C}_{iS} and \mathcal{C}_{iN} describe one pair of opposing sides and \mathcal{C}_{iW} and \mathcal{C}_{iE} the other pair. Let \mathcal{P}_{iSW} denote the point of intersection between the curves \mathcal{C}_{iS} and \mathcal{C}_{iW} , then a bijection $(x, y) = \mathcal{T}_i(\xi, \eta)$ from \mathcal{S} to \mathcal{B}_i is given by the transfinite interpolation

$$\begin{aligned} \mathcal{T}_i(\xi, \eta) &= (1 - \eta)\mathcal{C}_{iS} + \eta\mathcal{C}_{iN} + (1 - \xi)\mathcal{C}_{iW} + \xi\mathcal{C}_{iE} \\ &\quad - \xi\eta\mathcal{P}_{iNE} - \xi(1 - \eta)\mathcal{P}_{iSE} - \eta(1 - \xi)\mathcal{P}_{iNW} - (1 - \xi)(1 - \eta)\mathcal{P}_{iSW}. \end{aligned}$$

The unit square \mathcal{S} is discretized by the points

$$\begin{aligned}\xi_j &= jh_\xi, \quad h_\xi = 1/(N_{i\xi} - 1), \quad j = 0, \dots, N_{i\xi} - 1, \\ \eta_k &= kh_\eta, \quad h_\eta = 1/(N_{i\eta} - 1), \quad k = 0, \dots, N_{i\eta} - 1,\end{aligned}\tag{34}$$

where $N_{i\xi}$ and $N_{i\eta}$ are integers determining the number of grid points in the spatial directions of the discretization of the block \mathcal{B}_i . The corresponding grid points are computed as

$$(x_j, y_k) = \mathcal{T}_i(\xi_j, \eta_k).\tag{35}$$

We now give details on how each of the domains $\mathcal{D}_1 - \mathcal{D}_3$ are discretized. \mathcal{D}_1 is decomposed into five blocks $\mathcal{B}_1^{(1)} - \mathcal{B}_5^{(1)}$. The block $\mathcal{B}_1^{(1)}$ is a square at the center of the cylinder with corners at the points $(\pm ad, \pm ad)$, where a is the radius of the cylinder and $0 < d < 1$. Its bounding curves are

$$\begin{aligned}\mathcal{C}_{1S}^{(1)} &= a(2d\xi - d, -d), \\ \mathcal{C}_{1N}^{(1)} &= a(2d\xi - d, d), \\ \mathcal{C}_{1W}^{(1)} &= a(-d, 2d\eta - d), \\ \mathcal{C}_{1E}^{(1)} &= a(d, 2d\eta - d),\end{aligned}\tag{36}$$

The block $\mathcal{B}_2^{(1)}$ is defined by its bounding curves,

$$\begin{aligned}\mathcal{C}_{2S}^{(1)} &= \mathcal{C}_{1N}^{(1)}, \\ \mathcal{C}_{2N}^{(1)} &= a\left(\xi\sqrt{2} - \sqrt{1/2}, \sqrt{1 - (\xi\sqrt{2} - \sqrt{1/2})^2}\right), \\ \mathcal{C}_{2W}^{(1)} &= a(-\eta(1 - d) - d, \eta(1 - d) + d), \\ \mathcal{C}_{2E}^{(1)} &= a(\eta(1 - d) + d, \eta(1 - d) + d).\end{aligned}\tag{37}$$

The bounding curves of the remaining blocks $\mathcal{B}_3^{(1)} - \mathcal{B}_5^{(1)}$ that constitute \mathcal{D}_1 are obtained via

$$\mathcal{C}_{ij}^{(1)} = \mathcal{C}_{i-1j}^{(1)} \begin{bmatrix} \cos \pi/2 & \cos \pi/2 \\ \sin \pi/2 & -\sin \pi/2 \end{bmatrix}, \quad i = 3, 4, 5, \quad j = S, N, W, E.\tag{38}$$

\mathcal{D}_2 represents a cylindrical cavity in an infinite surrounding media and needs to be truncated in numerical computations. We construct the computational grid such that the cavity of radius a is centered inside a square of side $2D$. In this way \mathcal{D}_2 consists of four blocks $\mathcal{B}_1^{(2)} - \mathcal{B}_4^{(2)}$. The bounding curves of the block $\mathcal{B}_1^{(2)}$ are given by

$$\begin{aligned}\mathcal{C}_{2S}^{(1)} &= a\left(\xi\sqrt{2} - 1/\sqrt{2}, \sqrt{1 - (\xi\sqrt{2} - 1/\sqrt{2})^2}\right), \\ \mathcal{C}_{2N}^{(1)} &= (D, 2D\xi - D), \\ \mathcal{C}_{2W}^{(1)} &= \left(-\eta(D - a/\sqrt{2}) - a/\sqrt{2}, \eta(D - a/\sqrt{2}) + a/\sqrt{2}\right), \\ \mathcal{C}_{2E}^{(1)} &= \left(\eta(D - a/\sqrt{2}) + a/\sqrt{2}, \eta(D - a/\sqrt{2}) + a/\sqrt{2}\right),\end{aligned}\tag{39}$$

The bounding curves of the remaining blocks $\mathcal{B}_2^{(2)} - \mathcal{B}_4^{(2)}$ that constitute \mathcal{D}_2 are obtained via rotation by a factor $\pi/2$ as in (38).

The domain \mathcal{D}_3 consists of the union of the nine blocks that constitutes \mathcal{D}_1 and \mathcal{D}_2 . Figure 3 illustrates the grids used in this paper.

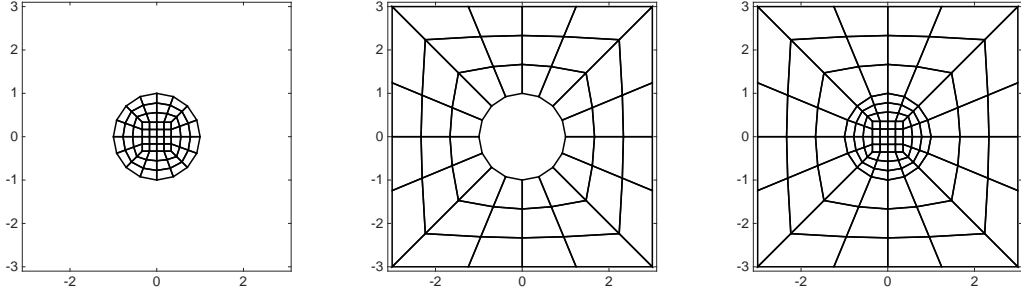


Figure 3: Structure of the grids used to discretize $\mathcal{D}_1, \mathcal{D}_2$ and \mathcal{D}_3 .

Remark 1. We note that the grids we use are not optimal and that it might be possible to obtain better results for the discontinuous Galerkin methods with an unstructured grid. The reason for using these block-structured grids is that it is easier to compare the results from different, structured and unstructured, methods.

5. Numerical Experiments

The particular solutions presented above provide non-trivial test problems for numerical methods that solve the elastic wave equation. The solutions were chosen to carefully test how well a numerical method can handle the boundary and interface conditions in the presence of a curved geometry.

Let $\mathbf{U}^{\text{num}}(t_k)$ and $\mathbf{U}^{\text{exact}}(t_k)$ be the numerical and the exact solution at time t_k . We define the relative maximum and L_2 errors

$$e_{\max}(t_k) = \frac{\|\mathbf{U}^{\text{num}}(t_k) - \mathbf{U}^{\text{exact}}(t_k)\|_{\infty}}{\max_{0 \leq t \leq T} \|\mathbf{U}^{\text{exact}}(t)\|_{\infty}}, \quad (40)$$

$$e_2(t_k) = \frac{\|\mathbf{U}^{\text{num}}(t_k) - \mathbf{U}^{\text{exact}}(t_k)\|_2}{\|\mathbf{U}^{\text{exact}}(0)\|_2}. \quad (41)$$

Note that the maximum norm is made relative by the max norm in space and over the computational time. To approximate the maximum norm we compute the maximum over discrete points on the grids, for the finite difference method these points are the grid points and for the discontinuous Galerkin method we sample the solution in a suitable number of (equidistant in (ξ, η)) points on each element. For the finite difference method the L_2 norm is approximated by a simple Riemann sum and for the discontinuous Galerkin method we use the Gaussian quadrature used to compute the elements of the mass and stiffness matrices.

5.1. Scattering of a Plane Wave

In this example we compute solutions to the plane wave scattering problem with the exterior solution (21) and, in the case of an inclusion, the interior solution (22).

In both cases the radius of the cylinder a is taken to be one, the frequency in time ω , entering (21)-(22) through the factor $e^{i\omega t}$, is set to 4π , and the material parameters outside the cylinder are set to $\lambda = \mu = \rho = 1$. For the case of an inclusion the material parameters inside the cylinder are $\lambda' = 1/2, \mu' = 1/10$ and $\rho' = 1$. The temporal period is $2\pi/\omega = 1/2$ and we solve the equations for 10 periods, i.e. until time 5. Initial data for this experiment is constructed by truncating the infinite series when the coefficients are zero to machine precision.

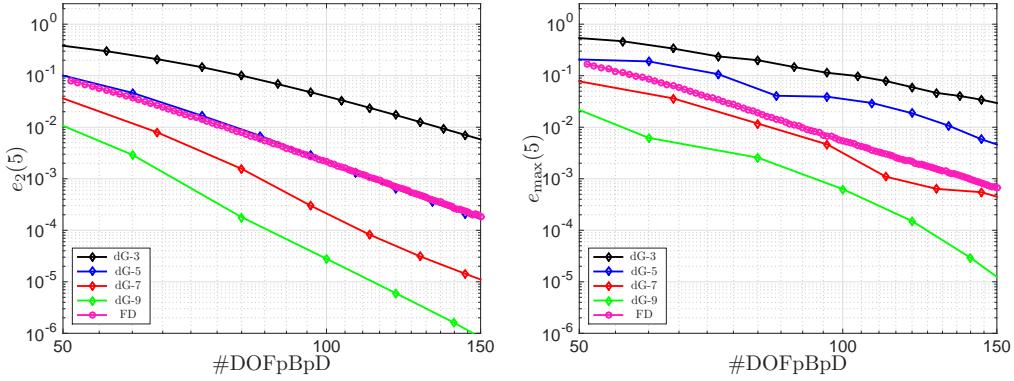


Figure 4: The cavity experiment. The discrete L_2 and maximum error for the discontinuous Galerkin methods and the finite difference method. The horizontal axis is displaying the number of degrees of freedom per block per dimension.

5.1.1. Results for the Cylindrical Cavity

The cavity is centered inside the square $[-3, 3] \times [-3, 3]$ (this corresponds to setting $D = 3$ in (39)). At the boundaries of the square the exact solution is imposed at all times and at the boundary of the cylinder a traction free boundary condition is imposed. Detailed descriptions how the boundary conditions are imposed for the two methods can be found in the references [12, 13, 27].

The computational grid is composed of the blocks $\mathcal{B}_2^{(i)}, i = 1 \dots 4$ discretized by $N_{i\xi} = N_{i\eta} = N$ points. To compare the finite difference method with discontinuous Galerkin methods using polynomials of degrees $q = 3, 5, 7, 9$ we compute solutions for a sequence of refined grids. In Figure 4 we report the maximum and L_2 errors for the different methods as a function of the number of degrees of freedom per block and per dimension, #DOFpBpD. For the finite difference method this is simply N and for the discontinuous Galerkin methods this is $N \times (q + 1)$.

The errors measured in the L_2 norm for the finite difference method and the dG method with $q = 5$ are almost identical. For the dG method with $q = 3$ the errors are bigger and for $q = 7$ and $q = 9$ they are smaller as expected. The observed rate of the convergence of the finite difference method is 6.00.

When the errors are measured in the maximum norm the finite difference method outperforms the dG method with $q = 3$ and $q = 5$ while the results obtained with the dG

method with $q = 7$ and $q = 9$ are still better than those obtained with the finite difference method. Overall, the convergence behavior of the finite difference method appears to be more robust than for the dG method. The observed rate of the convergence of the finite difference method is 5.47.

5.1.2. Results for the Cylindrical Inclusion

The discretization of the inclusion is composed of the blocks $\mathcal{B}_1^{(i)}, i = 1 \dots 5$. Here $\mathcal{B}_1^{(1)}$ is a square block with corners in the points $(\pm 1/\sqrt{8}, \pm 1/\sqrt{8})$ corresponding to letting $d = 1/\sqrt{8}$ in (36). As above we discretize all blocks by $N_{i\xi} = N_{i\eta} = N$ grid points in each direction.

As in the previous example the performance of the finite difference method is closest to the dG method with $q = 5$, in this case its errors are slightly better in the L_2 norm and significantly better, comparable to $q = 7$, in the maximum norm. As for the cavity the behavior of the error in the maximum norm is most robust for the finite difference method, which converges at a steady rate of 5.35. The convergence behavior in the L_2 norm is steady for all methods with the finite difference method converging at a rate of 6.14.

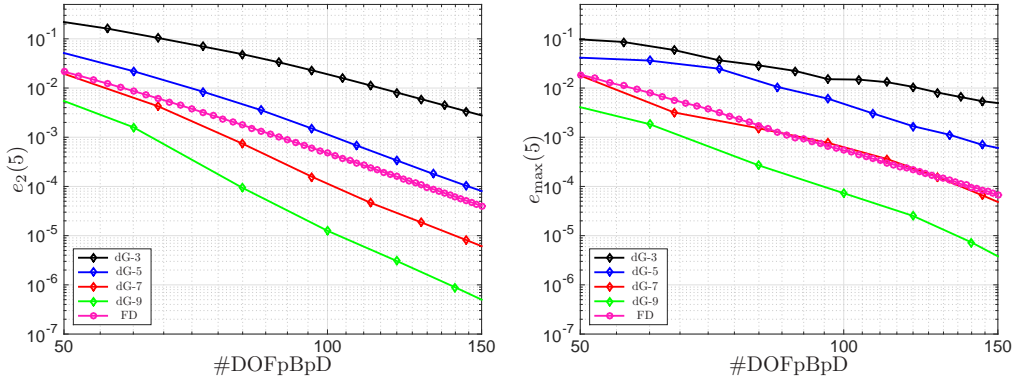


Figure 5: The inclusion experiment. The discrete L_2 and maximum error for the discontinuous Galerkin methods and the finite difference method.

5.2. Surface Waves on the Convex Boundary of an Elastic Cylinder

It has been shown by Kreiss and Petersson [29], that when approximated by finite difference methods, surface waves at the traction-free boundary of an elastic half-plane in numerical solutions of the elastic wave equation gives rise to discretization errors proportional to $(\lambda/\mu)^{(1/p)}$, where p is the order of accuracy of the finite difference method. In this experiment we investigate if this behavior is also observed for a curved boundary and for different methods.

We consider the harmonic motion of a single mode of the solution (25) inside a cylinder of radius $a = 1$ and with a wave number $k = 6$. We set $\lambda = \rho = 1$ and let μ assume values from the set $\{1, 0.1, 0.01, 0.001\}$. For each value of μ we compute the real valued roots of (30) ($D(c) = 0$) with $F_{ka} = J_{ka}$. The solution to the equation $D(c) = 0$ is not unique. In this section the smallest positive root for each value of μ is used. Having

computed c and setting $A = 1$ in (28) a corresponding value of B may be determined. The values of c used (as well as other roots) are tabulated in Table B.2 along with the corresponding values of B .

With $a = 1$, $k = 6$ the wavelength of the surface wave in the azimuthal direction at the boundary of the cylinder is $2\pi/6$. The variation the azimuthal and radial direction are of the same order for the cases considered in this experiment. To see this let n be an integer, then by the approximation

$$J_n(c\eta_s r) \approx \frac{1}{n!} \left(\frac{c\eta_s r}{2} \right)^n, \quad c\eta_s r \ll \sqrt{n+1}, \quad (42)$$

and the fact $c\eta_s = cka/\mu^{1/2} > cka/(\lambda+2\mu)^{1/2} = c\eta_p$, the variation in the radial direction is determined by the values of $c\eta_s$. The values of $c\eta_s$, tabulated in Table B.2, are all of the same magnitude hence the variation in both azimuthal and radial direction is of the same order for all cases considered in this experiment. The temporal period is $2\pi/(6c)$.

The initial data is computed from the real part of the expressions obtained by inserting (27) into (5) at the initial time $t = 0$. A plot of the magnitude of the displacement field at initial time is shown in Figure 2. The numerical solution is propagated for 6 temporal periods, after this time the waves has traversed the cylinder in the circumferential direction exactly once.

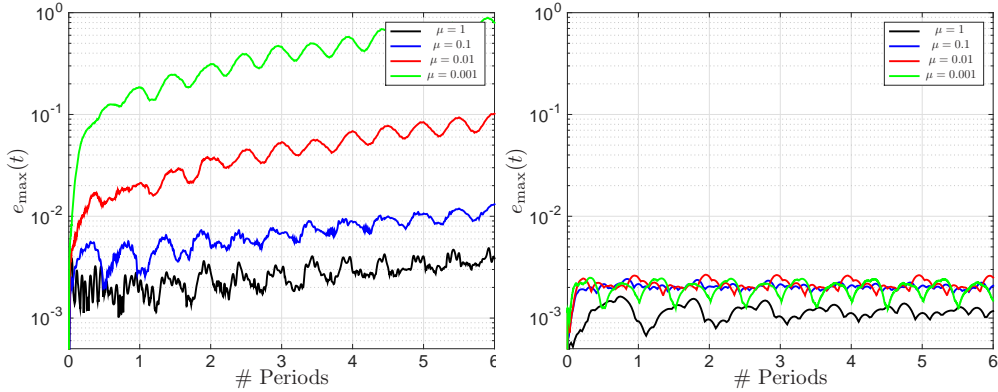


Figure 6: The maximum error as a function of time for a sequence of smaller values of μ using a fixed resolution of the surface wave, finite difference solution to the left and discontinuous Galerkin solution to the right.

5.2.1. Results

The computational grid is composed of the blocks $\mathcal{B}_i^{(1)}$, $i = 1, \dots, 5$. We let the square block $\mathcal{B}_1^{(1)}$ have its corners at the points $(\pm 1/\sqrt{8}, \pm 1/\sqrt{8})$ by taking $d = 1/\sqrt{8}$ in (36) and (37). For the finite difference method $\mathcal{B}_1^{(1)}$ is discretized with $N_{1\xi} = N_{1\eta} = 30$ points and $\mathcal{B}_i^{(1)}$, $i = 2, \dots, 5$ is discretized with $N_{2\xi} = 30$, $N_{2\eta} = 16$ grid points in each spatial direction. This yields a grid with 2820 degrees of freedom. This results in a grid that has the same grid spacing along the Cartesian coordinate axis and is conforming to the grid $\mathcal{B}_1^{(1)}$. This grid corresponds to 20 grid points per wavelength in the azimuthal

direction at the boundary of the cylinder and a resolution of about 30 grid points in the radial direction.

For the dG method we choose $q = 5$ and discretize all five blocks by 4×4 grids, i.e. we use $5 \times 4^4 \times 6^2 = 2880$ degrees of freedom.

The time-step used with the finite difference method is chosen as in [12] and is approximately $\Delta t = 4.9 \times 10^{-4}$, while the time step in the dG method is $\sim 2.4 \times 10^{-3}$ for $\mu = 1$ and increasing to $\sim 4.2 \times 10^{-3}$ for $\mu = 0.001$.

Figure 6 displays the maximum error as a function of time. For the finite difference method the error is about 2 magnitudes larger for $\mu = 0.001$ compared to $\mu = 1$ even though the wave is equally well resolved for both cases while for the discontinuous Galerkin method the results appear to be insensitive to μ .

5.3. Surface Waves on the Concave Boundary of a Cylindrical Cavity

As previously mentioned, the surface waves on a curved boundary are dispersive, i.e. $c = c(k)$. In this experiment we investigate how the maximum error depends on the wave number k .

For a cylinder of radius $a = 1$ we fix $\lambda = \mu = \rho = 1$ and let k take values from the set $\{2, 3, 4, 5, 6, 7, 8\}$. As in the previous example roots of the equation $D(c) = 0$ are computed, now for the different values of k and with $F_{ka} = H_{ka}^{(2)}$. Roots for waves that decay in time, i.e. with $\Im(c) > 0$, and values of B (computed with $A = 1$ in (28)-(29)) are tabulated in Table B.3 for the different values of k .

To keep the degrees of freedom per wavelength we must understand how the solution varies in the radial direction. For large values of $|c\eta_s r|$

$$H_n^{(2)}(c\eta_s r) \approx \sqrt{\frac{2}{\pi c\eta_s r}} e^{-i(\Re(c)\eta_s r - \frac{n\pi}{2} - \frac{\pi}{4})} e^{\Im(c)\eta_s r}, \quad (43)$$

thus the variation depends on the real and the imaginary part of $c\eta_s = \frac{cka}{\sqrt{\mu}}$. For the range of k we consider here, $2, \dots, 8$, we see from Table B.3 that the variation of $\Re c\eta_s$ is roughly 10 times larger than for $\Im c\eta_s$ and we therefor scale the discretization by $\Re c\eta_s$. Of course, the wavelength in the azimuthal direction, $r2\pi/k$, scales inversely with the wave number k .

The solution decays exponentially in time as $e^{-tka\Im(c)}$. We simulate until a time when the solution maximum is of 1% of the maximum of initial data, i.e. the final time is $T = -\frac{\ln 0.01}{ka\Im(c)}$.

5.3.1. Results

The computational grid used for the case of a cylindrical cavity is composed of the blocks $\mathcal{B}_2^{(i)}, i = 1 \dots 4$. The cavity is centered inside the square $[-3, 3] \times [-3, 3]$ which corresponds to letting $D = 3$ in (39).

At the boundary of the square the exact solution is imposed and at the boundary of the cylinder a traction free boundary condition is imposed.

For the finite difference method we discretize $\mathcal{B}_i^{(1)}, i = 1, \dots, 4$ with $N_{i\xi} = \lfloor 24k/2 \rfloor$ and $N_{i\eta} = \lfloor 16q_k \rfloor$ in (34), where $q_k = \frac{k\Re c(k)}{2\Re c(2)}$.

For the dG method we choose $q = 5$ i.e. the degrees of freedom per dimension is 6. To match the degrees of freedom to those of the finite difference method we choose

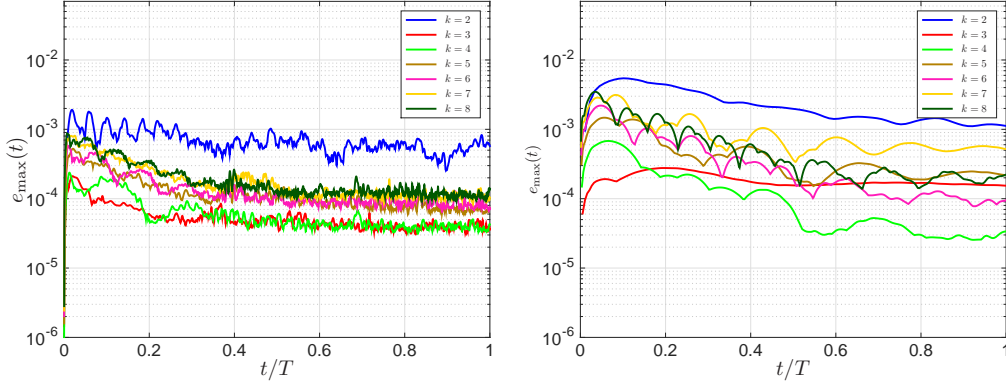


Figure 7: Left: Maximum error as a function of normalized time for the finite difference method. Right: Maximum error as a function of normalized time using the discontinuous Galerkin method with polynomials of degree 5. The results are for the example in §5.3.

$N_{i\xi} = \lfloor 4k/2 \rfloor$ and adjust $N_{i\eta}$. The exact values for $N_{i\eta}$ and $N_{i\xi}$ are tabulated in Table 1.

Table 1: Parameters for the different grids used in the experiments with the surface waves outside the cylinder.

q	2	3	4	5	6	7	8
FD $N_{i\xi}$	24	36	48	60	72	84	96
FD $N_{i\eta}$	16	44	72	100	129	157	186
# DOF (per block)	384	1584	3456	6000	9288	13188	17856
DG $N_{i\xi}$	4	6	8	10	12	14	16
DG $N_{i\eta}$	3	7	12	16	21	26	31
# DOF (per block)	432	1512	3456	5760	9072	13104	17856

Figure 7 displays the maximum errors as functions of t/T for each k in $\{2, 3, 4, 5, 6, 7, 8\}$. It can be seen that the errors for both methods are of the same magnitude indicating that there is no strong dependence on k . The errors are slightly better for the finite difference method for the number of periods considered here, however it also appears as if the errors decay faster over time for the dG method. The better long-time behavior of the dG method is another indication that the dispersive properties of the dG method are better than that of the finite difference method.

6. Summary

We have presented formulae for particular solutions to the elastic wave equation in cylindrical geometry. The solutions are freely available as the software **PeWe** which can be downloaded at [1].

The solutions were used to compare a finite difference and a discontinuous Galerkin method. The methods perform about equally well when $\lambda/\mu \sim 1$ but the discontinuous

Galerkin method out performs the finite difference method involving surface waves and $\lambda/\mu \gg 1$. The presented results can serve as a benchmark for future comparison using other numerical methods.

References

- [1] K. Virta, D. Appelö, <https://bitbucket.org/appelo/pewe> (2015).
- [2] W. Ewing, Elastic waves in layered media, McGraw-Hill series in the geological sciences, McGraw-Hill, 1957.
- [3] H. Lamb, On the propagation of tremors over the surface of an elastic solid, Philosophical Transactions of the Royal Society of London A: Mathematical, Physical and Engineering Sciences 203 (359-371) (1904) 1–42. doi:10.1098/rsta.1904.0013.
- [4] H. M. Mooney, Some numerical solutions for Lamb’s problem, Bulletin of the Seismological Society of America 64 (2) (1974) 473–491.
- [5] N. A. Petersson, B. Sjögreen, Super-grid modeling of the elastic wave equation in semi-bounded domains, Comm. Comput. Phys. 16 (2014) 913–955.
- [6] S. M. D. et al., Test of 3D elastodynamic codes: Final report for lifelines project 1A01, Tech. rep., Pacific Earthquake Engineering Center (2001).
- [7] L. C. Wilcox, G. Stadler, C. Burstedde, O. Ghattas, A high-order discontinuous Galerkin method for wave propagation through coupled elastic–acoustic media, Journal of Computational Physics 229 (24) (2010) 9373 – 9396.
- [8] D. Appelö, N. A. Petersson, A stable finite difference method for the elastic wave equation on complex geometries with free surfaces, Communications in Computational Physics 5 (1) (2009) 84–107.
- [9] M. Käser, M. Dumbser, An arbitrary high-order discontinuous Galerkin method for elastic waves on unstructured meshes - I. The two-dimensional isotropic case with external source terms, Geophysical Journal International 166 (2) (2006) 855–877.
- [10] B. Lombard, J. Piraux, C. Gelis, J. Virieux, Free and smooth boundaries in 2-D finite-difference schemes for transient elastic waves, Geophysical Journal International 172 (1) (2008) 252–261.
- [11] D. Appelö, J. W. Banks, W. D. Henshaw, D. W. Schwendeman, Numerical methods for solid mechanics on overlapping grids: Linear elasticity, Journal of Computational Physics 231 (18) (2012) 6012–6050.
- [12] K. Duru, K. Virta, Stable and high order accurate difference methods for the elastic wave equation in discontinuous media, Journal of Computational Physics 279 (2014) 37–62.
- [13] K. Duru, G. Kreiss, K. Mattsson, Stable and high-order accurate boundary treatments for the elastic wave equation on second-order form, SIAM Journal on Scientific Computing 36 (6) (2014) A2787–A2818.
- [14] D. Komatitsch, J.-P. Vilotte, The spectral element method; an efficient tool to simulate the seismic response of 2D and 3D geological structures, Bulletin of the Seismological Society of America 88 (2) (1998) 368–392.
- [15] B. Sjögreen, N. A. Petersson, A fourth order accurate finite difference scheme for the elastic wave equation in second order formulation, Journal of Scientific Computing 52 (1) (2012) 17–48.
- [16] E. Kausel, Fundamental solutions in elastodynamics: a compendium, Cambridge University Press, New York, 2006.
- [17] P. Berg, F. If, P. Nielsen, O. Skovgaard, Analytical reference solutions, Modeling the earth for oil exploration (1994) 421–427.
- [18] J. Diaz, A. Ezziani, Analytical solution for waves propagation in heterogeneous acoustic/porous media. Part I: the 2D case, Communications in Computational Physics 7 (1) (2010) 171.
- [19] K. Sezawa, Dispersion of elastic waves propagated on the surface of stratified bodies and on curved surfaces, Bulletin-Earthquake Research Institute (Tokyo) 3 (1927) 1–18.
- [20] H. Epstein, The effect of curvature on Stoneley waves, Journal of Sound and Vibration 46 (1) (1976) 59–66.
- [21] Y.-H. Pao, C. Mow, Scattering of plane compressional waves by a spherical obstacle, Journal of Applied Physics 34 (3) (1963) 493–499.
- [22] J. W. Miles, Motion of a rigid cylinder due to a plane elastic wave, The Journal of the Acoustical Society of America 32 (12) (1960) 1656–1659.
- [23] B. Strand, Summation by parts for finite difference approximations for d/dx , Journal of Computational Physics 110 (1) (1994) 47–67.

- [24] K. Mattsson, J. Nordström, Summation by parts operators for finite difference approximations of second derivatives, *Journal of Computational Physics* 199 (2) (2004) 503–540.
- [25] M. H. Carpenter, D. Gottlieb, S. Abarbanel, Time-stable boundary conditions for finite-difference schemes solving hyperbolic systems: methodology and application to high-order compact schemes, *Journal of Computational Physics* 111 (2) (1994) 220–236.
- [26] M. Svård, J. Nordström, On the order of accuracy for difference approximations of initial-boundary value problems, *Journal of Computational Physics* 218 (1) (2006) 333–352.
- [27] D. Appelö, T. Hagstrom, An energy-based discontinuous Galerkin discretization of the elastic wave equation in second order form, submitted to CMAME (2015).
- [28] D. Appelö, T. Hagstrom, https://bitbucket.org/appelo/dg_dath_elastic_v1.0 (2015).
URL \verb+https://bitbucket.org/appelo/dg_dath_elastic_v1.0+
- [29] H.-O. Kreiss, N. A. Petersson, Boundary estimates for the elastic wave equation in almost incompressible materials, *SIAM Journal on Numerical Analysis* 50 (3) (2012) 1556–1580.

Appendix A. Coefficients

The coefficients $m^{(ij)}$ and f_n^i of the linear systems of equations (23)-(24) are computed by substitution of the solutions (21)-(22) into the boundary or interface conditions (6)-(7). As a result these entries involves first and second derivatives of the present Bessel and Hankel functions. To solve the systems using numerical routines for computing values of Bessel and Hankel functions the coefficients of the linear systems are presented using the following recursion formula

$$\begin{aligned}\frac{d}{dr}J_n(\gamma r) &= \frac{\gamma}{2} (J_{n-1}(\gamma r) - J_{n+1}(\gamma r)), \\ \frac{d}{dr}H_n^{(2)}(\gamma r) &= \frac{\gamma}{2} (H_{n-1}^{(2)}(\gamma r) - H_{n+1}^{(2)}(\gamma r)).\end{aligned}\tag{A.1}$$

The coefficients of the equations (23) may be written

$$\begin{aligned}m_{11} &= (\lambda + 2\mu)\frac{\gamma_p^2}{4} (H_{n-2}^{(2)}(\gamma_p a) - 2H_n^{(2)}(\gamma_p a) + H_{n+2}^{(2)}(\gamma_p a)) \\ &\quad + \frac{\lambda}{a} \left(\frac{\gamma_p}{2} (H_{n-1}^{(2)}(\gamma_p a) - H_{n+1}^{(2)}(\gamma_p a)) - \frac{n^2}{a} H_n^{(2)}(\gamma_p a) \right), \\ m_{12} &= 2\mu\frac{n}{a} \left(\frac{\gamma_s}{2} (H_{n-1}^{(2)}(\gamma_s a) - H_{n+1}^{(2)}(\gamma_s a)) - \frac{1}{a} H_n^{(2)}(\gamma_s a) \right), \\ m_{21} &= 2\mu\frac{n}{a} \left(\frac{1}{a} H_n^{(2)}(\gamma_p a) - \frac{\gamma_p}{2} (H_{n-1}^{(2)}(\gamma_p a) - H_{n+1}^{(2)}(\gamma_p a)) \right), \\ m_{22} &= -n^2\frac{\mu}{a^2} H_n^{(2)}(\gamma_s a) - \mu\frac{\gamma_s^2}{4} (H_{n-2}^{(2)}(\gamma_s a) - 2H_n^{(2)}(\gamma_s a) + H_{n+2}^{(2)}(\gamma_s a)) \\ &\quad + \frac{\mu}{a}\frac{\gamma_s}{2} (H_{n-1}^{(2)}(\gamma_s a) - H_{n+1}^{(2)}(\gamma_s a)), \\ f_1 &= (\lambda + 2\mu)\frac{\gamma_p^2}{4} (J_{n-2}(\gamma_p a) - 2J_n(\gamma_p a) + J_{n+2}(\gamma_p a)) \\ &\quad + \frac{\lambda}{a} \left(\frac{\gamma_p}{2} (J_{n-1}(\gamma_p a) - J_{n+1}(\gamma_p a)) + -\frac{n^2}{a} J_n(\gamma_p a) \right), \\ f_2 &= 2\mu\frac{n}{a} \left(\frac{1}{a} J_n(\gamma_p a) - \frac{\gamma_p}{2} (J_{n-1}(\gamma_p a) - J_{n+1}(\gamma_p a)) \right).\end{aligned}\tag{A.2}$$

The coefficients of the equations (24) may be written

$$\begin{aligned}
m_n^{(11)} &= \frac{\gamma_p}{2} \left(H_{n-1}^{(2)}(\gamma_p a) - H_{n+1}^{(2)}(\gamma_p a) \right), \\
m_n^{(12)} &= \frac{n}{a} H_n^{(2)}(\gamma_s a), \\
m_n^{(13)} &= -\frac{\gamma'_p}{2} \left(J_{n-1}(\gamma'_p a) - J_{n+1}(\gamma'_p a) \right), \\
m_n^{(14)} &= -\frac{n}{a} J_n(\gamma_s a), \\
m_n^{(21)} &= -\frac{n}{a} H_n^{(2)}(\gamma_p a), \\
m_n^{(22)} &= -\frac{\gamma_s}{2} \left(H_{n-1}^{(2)}(\gamma_s a) - H_{n+1}^{(2)}(\gamma_s a) \right), \\
m_n^{(23)} &= \frac{n}{a} J_n(\gamma'_p a), \\
m_n^{(24)} &= -\frac{\gamma_s}{2} \left(J_{n-1}(\gamma_s a) - J_{n+1}(\gamma_s a) \right), \\
m_n^{(31)} &= (\lambda + 2\mu) \frac{\gamma_p^2}{4} \left(H_{n-2}^{(2)}(\gamma_p a) - 2H_n^{(2)}(\gamma_p a) + H_{n+2}^{(2)}(\gamma_p a) \right) \\
&\quad + \frac{\lambda}{a} \left(\frac{\gamma_p}{2} \left(H_{n-1}^{(2)}(\gamma_p a) - H_{n+1}^{(2)}(\gamma_p a) \right) - \frac{n^2}{a} H_n^{(2)}(\gamma_p a) \right), \\
m_n^{(32)} &= 2\mu \frac{n}{a} \left(\frac{\gamma_s}{2} \left(H_{n-1}^{(2)}(\gamma_s a) - H_{n+1}^{(2)}(\gamma_s a) \right) - \frac{1}{a} H_n^{(2)}(\gamma_s a) \right), \\
m_n^{(33)} &= -(\lambda' + 2\mu') \frac{\gamma_p'^2}{4} \left(J_{n-2}(\gamma'_p a) - 2J_n(\gamma'_p a) + J_{n+2}(\gamma'_p a) \right) \\
&\quad - \lambda' \left(\frac{1}{a} \frac{\gamma'_p}{2} \left(J_{n-1}(\gamma'_p a) - J_{n+1}(\gamma'_p a) \right) - \frac{n^2}{a^2} J_n(\gamma'_p a) \right), \\
m_n^{(34)} &= -2\mu' \frac{n}{a} \left(\frac{\gamma'_s}{2} \left(J_{n-1}(\gamma'_s a) - J_{n+1}(\gamma'_s a) \right) - \frac{1}{a} J_n(\gamma'_s a) \right), \\
m_n^{(41)} &= 2\mu \frac{n}{a} \left(\left(\frac{1}{a} H_n^{(2)}(\gamma_p a) - \frac{\gamma_p}{2} \left(H_{n-1}^{(2)}(\gamma_p a) - H_{n+1}^{(2)}(\gamma_p a) \right) \right) \right), \\
m_n^{(42)} &= -\mu \left(\frac{n^2}{a} H_n^{(2)}(\gamma_s a) + \frac{\gamma_s^2}{4} \left(H_{n-2}^{(2)}(\gamma_s a) - 2H_n^{(2)}(\gamma_s a) + H_{n+2}^{(2)}(\gamma_s a) \right) \right) \\
&\quad + \frac{\mu}{a} \frac{\gamma_s}{2} \left(H_{n-1}^{(2)}(\gamma_s a) - H_{n+1}^{(2)}(\gamma_s a) \right), \\
m_n^{(43)} &= -2\mu' \frac{n}{a} \left(\left(\frac{1}{a} J_n(\gamma'_p a) - \frac{\gamma'_p}{2} \left(J_{n-1}(\gamma'_p a) - J_{n+1}(\gamma'_p a) \right) \right) \right), \\
m_n^{(44)} &= \mu' \left(\frac{n^2}{a} J_n(\gamma'_s a) + \frac{\gamma_s'^2}{4} \left(J_{n-2}(\gamma'_s a) - 2J_n(\gamma'_s a) + J_{n+2}(\gamma'_s a) \right) \right) \\
&\quad - \frac{\mu'}{a} \frac{\gamma'_s}{2} \left(J_{n-1}(\gamma'_s a) - J_{n+1}(\gamma'_s a) \right) \\
f_n^{(1)} &= \frac{\gamma_p}{2} \left(J_{n-1}(\gamma_p a) - J_{n+1}(\gamma_p a) \right), \\
f_n^{(2)} &= -\frac{n}{a} J_n(\gamma_p a), \\
f_n^{(3)} &= (\lambda + 2\mu) \frac{\gamma_p^2}{4} \left(J_{n-2}(\gamma_p a) - 2J_n(\gamma_p a) + J_{n+2}(\gamma_p a) \right) \\
&\quad + \lambda \left(\frac{1}{a} \left(J_{n-1}(\gamma_p a) - J_{n+1}(\gamma_p a) \right) - \frac{n^2}{a^2} J_n(\gamma_p a) \right), \\
f_n^{(4)} &= 2\mu \frac{n}{a} \left(\frac{1}{a} J_n(\gamma_p a) - \frac{\gamma_p}{2} \left(J_{n-1}(\gamma_p a) - J_{n+1}(\gamma_p a) \right) \right).
\end{aligned} \tag{A.3}$$

Appendix B. Tabulated constants

μ	c	B
1	* 1.118807339314738	$i0.259859421131935$
1	1.766356057610045	$i0.551757806713995$
1	2.185554978245760	$-i1.111726166772277$
1	2.670175822539088	$i0.958432243767886$
1	2.955157420561863	$-i0.732513991983086$
0.1	* 0.362343233711522	$i0.008979356435568$
0.1	0.579278221572536	$i0.061797475082992$
0.1	0.728953134331886	$-i0.195334916685379$
0.1	0.895978188422108	$i0.716217080313942$
0.1	1.067385352879540	$-i1.855812650827352$
0.01	* 0.115042076979121	$i1.800969171774775 \times 10^{-5}$
0.01	0.184047312259251	$i1.608778558352172 \times 10^{-4}$
0.01	0.232136819580657	$-i5.996559491070863 \times 10^{-4}$
0.01	0.284650355722595	$i0.002791241585515$
0.01	0.338604827125379	$-i0.010369491587158$
0.001	* 0.036395018364438	$i1.946610327968597 \times 10^{-8}$
0.001	0.058228929768223	$i1.791032555369920 \times 10^{-7}$
0.001	0.073461004595573	$-i6.806632052120861 \times 10^{-7}$
0.001	0.090056708451170	$i3.250907109941674 \times 10^{-6}$
0.001	0.107108691805566	$-i1.252501580039413 \times 10^{-5}$

Table B.2: The computed values of c and B for all values of μ used in the example with surface waves inside a cylinder. The values marked by the symbol * are used in the computations that are presented.

k	c	B
2	$0.247859606990339 + i0.241244901429628$	$-0.119481693313368 - i2.996924150548532$
3	$0.458766909774936 + i0.187333825635153$	$-0.433288418131060 - i4.741971316305029$
4	$0.561991684435237 + i0.148828718025219$	$-0.908447005479862 - i7.300093250067868$
5	$0.624468663833749 + i0.122118151982478$	$-1.634838389505964 - i11.096286394747006$
6	$0.666789891576908 + i0.102736201288173$	$-2.741262468068052 - i16.740023608389567$
7	$0.697581719963342 + i0.088096812705306$	$-4.415934969322963 - i25.126574554563344$
8	$0.721118660968997 + i0.076679428531871$	$-6.934676718614770 - i37.575882485238743$

Table B.3: The computed values of c and B for all values of k used in the example with surface waves outside a cylinder.